Earth and Planetary Science Letters 537 (2020) 116200

Contents lists available at ScienceDirect

Earth and Planetary Science Letters

www.elsevier.com/locate/epsl

A recent increase in megathrust locking in the southernmost rupture area of the giant 1960 Chile earthquake

Haipeng Luo [a], Boudewijn Ambrosius [b], Raymond M. Russo [c], Victor Mocanu [d], Kelin Wang [e,a,*], Michael Bevis [f], Rui Fernandes [g]

[a] School of Earth and Ocean Sciences, University of Victoria, Victoria, British Columbia, Canada
[b] Faculty of Aerospace Engineering, Delft University of Technology, Kluyverweg 1, 2629 HS, Delft, the Netherlands
[c] Department of Geological Sciences, University of Florida, Gainesville, FL 32608, USA
[d] Department of Geophysics, University of Bucharest, 6 Traian Vuia Street, RO-020956, Bucharest, Romania
[e] Pacific Geoscience Centre, Geological Survey of Canada, 9860 West Saanich Road, Sidney, British Columbia, Canada
[f] School of Earth Sciences, Ohio State University, 125 South Oval Mall, Columbus, OH 43210, USA
[g] University of Beira Interior, Instituto D. Luiz, Rua Marquês d'Ávila e Bolama, 6201-001 Covilhã, Portugal

ARTICLE INFO

Article history:
Received 29 September 2019
Received in revised form 12 February 2020
Accepted 28 February 2020
Available online 13 March 2020
Editor: J.-P. Avouac

Keywords:
subduction earthquake
postseismic deformation
viscoelastic stress relaxation
enhanced megathrust locking
great 1960 Chile earthquake

ABSTRACT

After a great subduction earthquake, viscoelastic stress relaxation causes prolonged seaward motion of inland areas of the upper plate, as was observed around the turn of the century in the area of the 1960 Mw 9.5 Chile earthquake with Global Navigation Satellite System (GNSS) measurements. However, recent GNSS observations during 2010–2019 indicate a systematic decrease in the velocity of the seaward motion over a region covering the latitudinal range of the southern half of the 1960 rupture. Data from the only long-lived continuous site in this region (COYQ since 1997), situated over 200 km away from the trench, suggest that the decrease in the seaward velocity (or increase in the landward velocity) occurred within a few years prior to 2010. This rapid and regional change cannot be explained by viscoelastic relaxation. We thus propose that the change was caused by a relatively sudden downdip widening of the zone of locking along the megathrust. Using three-dimensional finite element modelling, we find that the observed velocity change cannot be otherwise explained, although the amount of the increase in locking cannot be uniquely determined because of trade-offs between, and uncertainties in, the various parameters involved. For example, the degree of the increase in locking is affected by the value of coseismic slip in 1960 in the southernmost part of the rupture zone. A postseismic deformation model with greater coseismic slip in accordance with the most recent coseismic slip model in the literature better fits COYQ data prior to 2005 and requires greater locking increase afterwards. A model with less coseismic slip requires less locking increase but an additional long-term slow slip event prior to 2005. The rapid surface velocity change and the inferred increase in megathrust locking several decades after a great earthquake present new challenges to the understanding of fault mechanics and subduction zone dynamics.

1. Introduction

The geodetically observed evolution of crustal deformation following a subduction earthquake is understood to be controlled by the combined effects of viscoelastic mantle rheology, fault creep such as afterslip, and relocking of the megathrust. Immediately after a great earthquake, the trench area and areas farther landward exhibit opposing motion, as illustrated by the motion of sites A and B at stage t_1 in Fig. 1. This is mostly a consequence of viscoelastic relaxation of the stress induced by the earthquake (Sun et al., 2014; Sun and Wang, 2015), although afterslip downdip of the rupture zone can also play an important role (Pritchard and Simons, 2006). As the effect of the viscoelastic relaxation diminishes with time and the effect of fault locking becomes more dominant, the boundary dividing the regions of opposing motion gradually migrates landward, eventually leading to wholesale landward motion of the upper plate (Wang et al., 2012) (Fig. 1). The time it takes to complete the process of motion reversal depends on the magnitude of the earthquake, as demonstrated by Sun et al. (2018)

* Corresponding author at: Pacific Geoscience Centre, Geological Survey of Canada, 9860 West Saanich Road, Sidney, British Columbia, Canada.
E-mail addresses: hpluo@uvic.ca (H. Luo), b.a.c.ambrosius@tudelft.nl (B. Ambrosius), rrusso@ufl.edu (R.M. Russo), victor.mocanu@g.unibuc.ro (V. Mocanu), kelin.wang@canada.ca (K. Wang), bevis.6@osu.edu (M. Bevis), rui@segal.ubi.pt (R. Fernandes).

https://doi.org/10.1016/j.epsl.2020.116200

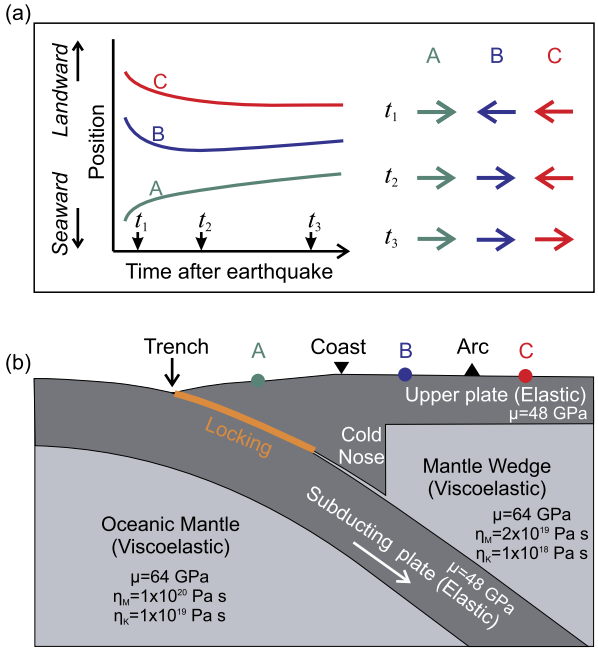

Fig. 1. Schematic illustration of postseismic deformation of subduction earthquakes. (a) Modified from Sun et al. (2018). Left: Evolution of postseismic displacement at the three sites marked in (b). Right: Velocity direction of the three sites at three stages of the postseismic deformation, showing landward migration of the dividing boundary of opposing motion. (b) Structure and parameter values of the numerical model used in Sun et al. (2018) and this work to model the postseismic deformation of the 1960 Chile earthquake. Here μ and η are rigidity and viscosity, respectively, and subscripts K and M denote the Kelvin and Maxwell components of the bi-viscous transient rheology. The Poisson's ratio is assumed to be uniformly 0.25. (For interpretation of the colours in the figure(s), the reader is referred to the web version of this article.)

using geodetic observations and viscoelastic deformation models of great subduction earthquakes worldwide. For events of moment magnitude (Mw) 8, the reversal takes about a decade or so; for Mw $>$ 9 events, this process can take an order of magnitude longer.

The largest magnitude earthquake yet recorded instrumentally, the Mw 9.5 1960 Chile earthquake, ruptured the Nazca–South America subduction interface over a distance of 920 $\pm$ 100 km, from Valdivia in the north to the Nazca–Antarctica–South America triple junction in the south (Cifuentes, 1989), with coseismic slip estimates up to 40 m (Plafker and Savage, 1970; Barrientos and Ward, 1990; Moreno et al., 2009). Recent analysis of the records of the tsunami generated by this earthquake confirmed the large coseismic slip (Ho et al., 2019).

Analyses of Global Navigation Satellite Systems (GNSS) measurements four decades after the 1960 Chile earthquake (Klotz et al., 2001; Khazaradze et al., 2002; Wang et al., 2007; Moreno et al., 2011) showed opposing motion at campaign GNSS sites some 200–300 km from the Nazca trench (Fig. 2), much like the t_2 stage in Fig. 1a. The research groups that made the GNSS observations shown in Fig. 2 each used a slightly different definition of the South America (SA) reference frame, but the resultant differences in the derived velocities are negligibly small for the purpose of studying regional postseismic and interseismic deformation. The observed deformation pattern is reasonably well explained as a snapshot of a deformation history predicted using a spherical-Earth viscoelastic finite element model (Sun et al., 2018) (Fig. 2). The viscoelastic modelling shows that the westward (trenchward or seaward) motion of the area 200–300 km east of the trench and farther away is not expected to diminish or to reverse direction until 90–100 yrs post coseismic rupture ($\sim$ mid 21st C.) (Hu et al., 2004; Wang et al., 2012; Sun et al., 2018). However, we show in this paper that more recent GNSS observations made in the early 21st century indicate unexpectedly early deceleration of seaward velocities or even reversal of crustal motion in this area, indicating an earlier than expected transition from the t_2 to t_3 stages illustrated in Fig. 1a.

2. Geodetic observations

2.1. Two-decade displacement history at site COYQ

The GNSS velocities shown in Fig. 2a were obtained with campaign measurements. There were few continuously monitoring stations in the 1990's and 2010's in South America in the latitudinal range of the 1960 Chile earthquake. Within our study area (south of 42.5°), COYQ was the only continuous station until 2009. The westward motion of COYQ since its establishment in 1997 is consistent with the general pattern of postseismic deformation of giant subduction earthquakes outlined in the Introduction. However, the temporal changes in its velocity have presented surprises.

Fig. 3 shows weekly position solutions of COYQ over the past 20 yrs relative to the SA reference frame defined by minimizing the motion of the seven continuous GNSS sites shown in Fig. 4. For data processing, we employ the GIPSY-OASIS v.6.4 software and use the precise point positioning (PPP) strategy (Zumberge et al., 1997) to generate daily position solutions. We use the Jet Propulsion Laboratory (JPL), Pasadena, orbits and clocks, as well as the widelane ambiguity products, to invoke single station ambiguity fixing (Bertiger et al., 2010). The resultant non-fiducial position solutions are then transformed into the ITRF2014 International Terrestrial Reference Frame, using a global Helmert seven-parameter transformation also provided by JPL along with the orbits and clocks. We have combined the daily solutions into weekly position estimates for Fig. 3. One of us (MB) independently processed the same data using a procedure as previously described in Kendrick et al. (2001) and Brooks et al. (2003) and obtained nearly identical results. The most intriguing signal in the COYQ time series is the rapid deceleration of westward motion which began before 2010 (Fig. 3a).

The COYQ site position time series shown in Fig. 3 exhibit long-term trends with clear seasonal variations that are common in time series solutions of GNSS stations. Because the primary deformation signals examined in this work vary on a timescale of several years or decades, we choose to show the original time series in Fig. 3 without removing the seasonal variations. The seasonal variations can be crudely quantified using sinusoidal functions as discussed in Appendix A, with parameters given in Table B1.

The motion of COYQ was affected by the coseismic and/or postseismic deformation of the 2010 Mw 8.8 Maule, 2015 Mw 8.3 Illapel, and the 2016 Mw 7.7 Quellón earthquakes to variable degrees ranging from negligible to significant. These three earthquakes were megathrust rupture events along the Nazca–South America subduction zone (Fig. 4). As explained in Appendix A, we quantify coseismic jump and postseismic motion of COYQ caused by these events by fitting step and exponential functions to the time series, with parameters given in Table B1. For the purpose of this study, we focus on the east–west component, which is noticeably affected only by the nearby 2016 Mw 7.7 Quellón earthquake. The earthquake caused a 3.85 mm coseismic westward jump of COYQ (Fig. 3a and Appendix A), but it has no impact on the main signal discussed in this paper, the deceleration of westward motion starting before 2010. The other two earthquakes occurred over 1000 km away. They had minor or negligible impact on the east–west component but somewhat greater impact on the north–south component, in particular postseismic motion following the 2010 Maule earthquake as highlighted in Fig. 3b (Table B1).

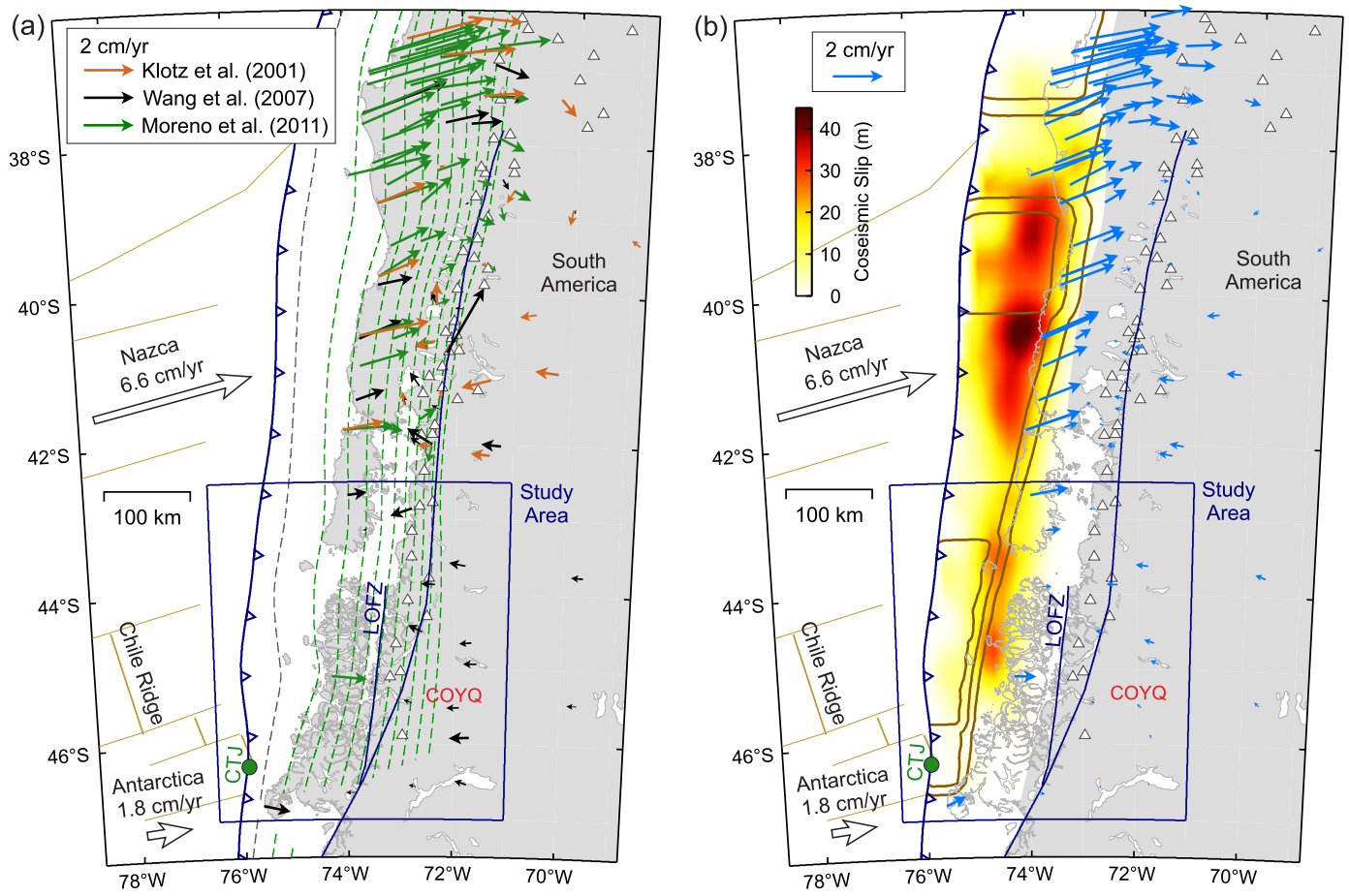

Fig. 2. Observed and model-predicted GNSS site velocities. (a) GNSS velocities based on campaign surveys of 1994–1996 (Klotz et al., 2001), 1994–2005 (Wang et al., 2007), and 2002–2009 (Moreno et al., 2011). Displacement time series of site COYQ (red labelled) are shown in Fig. 3. LOFZ, Liquiñe-Ofqui fault zone (Cembrano et al., 2002). CTJ, Chile triple junction. Sites west of LOFZ have been corrected for strike-parallel sliver motion following Wang et al. (2007). (b) Velocities 40 yrs after the 1960 Mw 9.5 Chile earthquake predicted by the postseismic deformation model of Sun et al. (2018). The 1960 coseismic slip distribution employed by this model was estimated by Moreno et al. (2009). In this figure and other map view figures in this paper, depth below sea level of the megathrust (interrupted by a slab window in the south) is contoured using dashed green lines at 10 km intervals, and slip deficit rates (Sun et al., 2018) are contoured using brown solid lines at 2 cm/yr intervals.

Instrument failure in 2005 and 2007 caused data gaps (Fig. 3). The ensuing station repair in 2007 gave rise to the possibility of a phase centre shift. Upon visual inspection of the original east–west time series, there appears to be an upward (east) shift of about 4 mm in 2007 (Fig. 3a). Despite lack of detailed documentation of the station repair in 2007, we address the uncertainties in this possible offset: We show the east–west time series with downward (west) offsets of 0, 4, and 8 mm in Fig. 3a. As explained in section 3.2, these uncertainties slightly affect some of our interpretation.

At the location of COYQ, the strongest postseismic effect of the 1960 earthquake is in the margin-normal direction, manifested as long-lasting seaward (westward) motion. However, the velocity of the westward motion (general slope of the curve) decreased rather quickly from a few years before 2010 and then began to show some eastward motion. The aforementioned data gaps and station repair during 2005–2007 should not affect the velocity estimates before 2005 and after 2007. There is indication that the southward motion of the site may have become slightly faster around 2005 (Fig. 3b), but data gaps in 2005 and 2007 and the perturbation caused by the 2010 Maule earthquake make it difficult to decipher more quantitative information.

The velocity change at COYQ presents a serious scientific challenge. Viscoelastic earthquake cycle models based on realistic upper mantle viscosities predict that surface sites at distances of 200–300 km from the 1960 Chile earthquake rupture zone should continue to move trenchward (west) on a centennial time scale. Thus, in 2019, nearly 60 yrs post event, we would expect trenchward motion at COYQ to persist for three to four more decades. Furthermore, these models show that the eventual site velocity reversal from trenchward to landward should be very gradual (Hu et al., 2004; Wang et al., 2012; Sun et al., 2018). No reasonable model of viscoelastic stress relaxation can explain the observed early and rapid deceleration of trenchward motion and the apparent premature velocity reversal at COYQ.

2.2. A regional increase in eastward velocity

Do the rapid deceleration and reversal of COYQ represent a regional change reflecting some actual subduction zone process or a local effect associated with site stability or small-scale geological processes? The question cannot be answered by observations from a single site. Therefore, we installed 4 new continuously recording GNSS stations in 2013–2015 (SAJA, BBAF, TRQ2, LSAR) (Fig. 5a). The available data (with occasional gaps due to data dropouts) were processed until March 2019 (Table B2). We also processed daily position solutions computed by Blewitt et al. (2018) from 8 other stations in our study area (ESQU, FUTF, QLLN, RMBA, MELK, TPYU, BN11 and XPLO) (Fig. 5a), spanning approximately 2010–2019 (Table B2). The data processing procedure for these 12 stations is the same as described in section 2.1 and Appendix A for COYQ. We derived site velocities averaged over each station's data span using a

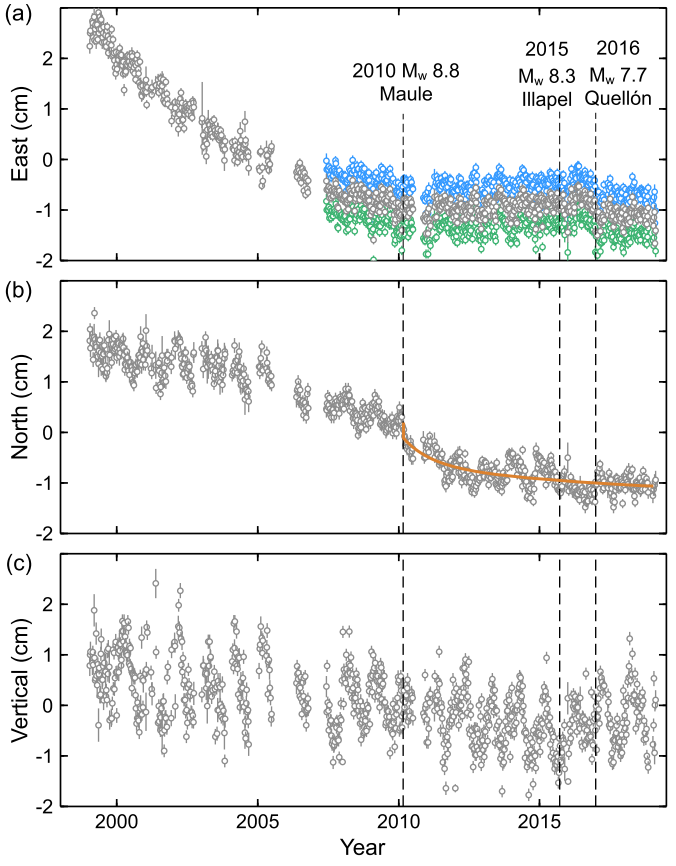

Fig. 3. Time history of weekly position of GNSS site COYQ relative to the SA reference defined in this work (Fig. 4) showing rapid velocity change in the early 21st century. Error bars represent 3 standard deviations. Locations of the three marked earthquakes are shown in Fig. 4. For this display, no corrections are applied for seasonal variations and perturbations caused by the shown earthquakes (Appendix A). (a) East component, which is the focus of this work. Data after site repair in 2007 are shown in blue, grey, and green for three possible offset values 0, −4, and −8 mm, respectively, as explained in section 2.1. (b) North component. Orange line highlights coseismic and postseismic effects of the 2010 Maule earthquake (Appendix A). (c) Vertical component.

simple linear model. In Fig. 5, these new velocities are compared with the earlier velocities reported by Wang et al. (2007) based on campaign GNSS observations between 1994–2005.

Given variable data recording conditions that reflect differences in GNSS station equipment and monument design, the effects of large earthquakes in South America, different time spans of observation, and the crude manner by which dextral motion of the Liquiñe-Ofqui fault zone (LOFZ) was corrected (Wang et al., 2007), we refrain from detailed interpretations of the magnitudes and directions of individual velocity vectors shown in Fig. 5a. However, it is remarkable that the 2010–2019 data collectively exhibit a regional increase in eastward velocity (or decrease in westward velocity) when compared to the 1994–2005 data (Fig. 5c). Velocity values from individual sites that provided data during both time periods, or different sites from different periods but located at similar distances from the 1960 earthquake rupture zone, consistently show an increase in eastward velocity. Fig. 5c only includes sites east of the 50 km depth contour of the plate interface (Hayes et al., 2012) for convenience of graphical display; however, stations west of the contour, such as MELK and QLLN, also show a similar eastward increase in site velocity. This systematic change strongly suggests that the striking velocity change visible in ∼ 20 yrs of COYQ data (Fig. 3a) reflects a regional increase in eastward velocity.

The regional velocity change seen in Fig. 5c cannot be an artefact due to differences between our stable SA reference frame and that of Wang et al. (2007). Most of the sites used by Wang et al. (2007) to define the SA reference are no longer operating, making it impossible to reproduce their results exactly. However, the comparison in Fig. 4 demonstrates that their SA reference is practically identical to the SA reference we have defined in this work. Fig. 4 shows velocity residuals for our sites in our new reference frame and also for their sites in their reference frame; the residuals would be identically zero if all the sites were on an ideally rigid plate and the GNSS data were error free. For sites used by both groups (KOUR or BRAZ) or located not very far apart (BRFT and FORT or CHPI and VICO), the vectorial difference between the two residuals is well below 1 mm/yr, and the directional difference is random. Therefore, the reference frame difference between our work and Wang et al. (2007) cannot possibly cause the systematic eastward velocity shift of around 5 mm/yr in our study area (Fig. 5c).

The regional change in Fig. 5c cannot be an effect of the 2010 Mw 8.8 Maule earthquake (Fig. 4). First, the velocity change at COYQ mostly occurred before 2010, and it is difficult to credit the notion that the site motions in our area – some 1000 km from the Maule rupture zone – were a slow preparatory phase of the Maule event. Second, in our study area, the influence of the co- and post-seismic motions due to the Maule earthquake is mainly in the north–south direction (Fig. 3b).

The regional change shown in Fig. 5c cannot be associated with changes in surface loading due to non-tectonic processes. Seasonal and multi-year surface and ground hydrological changes are known to induce both vertical and horizontal crustal motion (Amos et al., 2014; Kreemer and Zaliapin, 2018), commonly with much stronger effect on vertical than horizontal motions. Some of the GNSS sites in Fig. 5, especially those near the coast and in the southern part of the study area, indeed exhibit faster vertical than horizontal motion. However, the velocity difference between the two measurement periods for nearby sites is generally much smaller on the vertical velocity component. If hydrological loading in this area (e.g., Rodell et al., 2018) is responsible for the faster vertical motion, it must be operating at a timescale long enough to affect both measurement periods similarly and cannot be the main cause for the rapid velocity change between the two periods which is predominantly horizontal. The effects of climatically induced changes in ice loading are more important south of our study region (Dietrich et al., 2010; Richter et al., 2016) and deserve more detailed research.

We thus must conclude that the sudden increase in eastward velocity in the early 21st century, both at COYQ and at a regional scale, is a true tectonic signal. Given reasonable ranges of mantle viscosity, it is not possible to explain either the rapidity of this velocity change, nor its early occurrence relative to modelling predictions, as part of the normal postseismic deformation process of the great 1960 Chile earthquake. We considered and dismissed as very unlikely complex transient or nonlinear Earth rheology that might be invoked to explain the observed rapid regional velocity change. The only remaining possibility commensurate with the time scale of this observed velocity change is a change in the state of interplate locking. Thus, in the ensuing section we explore the effects of an increase in the degree of locking of the subduction megathrust in our study region that developed within a few years prior to 2010.

3. Case for a recent increase in megathrust locking

3.1. The finite element model

Our model builds on that of Sun et al. (2018) for the 1960 Chile earthquake, based on coseismic slip estimates from Moreno et al. (2009), except that we have slightly modified the model trench

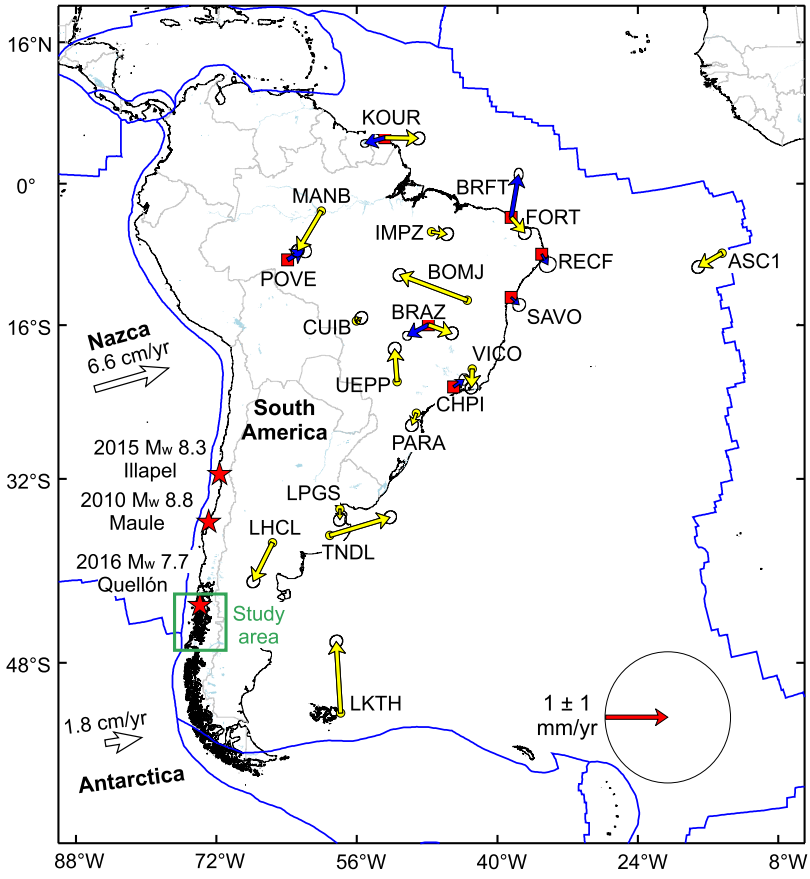

Fig. 4. Definition of the South America (SA) reference frame. Red squares show stations used to define the SA reference in this work, and blue arrows show their motion in this reference frame. For comparison, stations used to define the SA reference by Wang et al. (2007) and their motion in that reference frame are shown with yellow circles and arrows, respectively. Blue lines outline plate boundaries, and light grey lines show international boundaries. Nazca and Antarctica plate velocities are from Argus et al. (2010). The three earthquakes marked with stars affected the COYQ time series to different degrees (Fig. 3).

geometry to take advantage of a new algorithm we employ to generate the finite element mesh in the spherical Earth. However, we have also constructed a model that uses the newly published coseismic slip distribution of Ho et al. (2019) as detailed in the following section. We refer the reader to Sun et al. (2018) for model details but highlight the following points.

Our Earth model assumes that the mantle obeys the bi-viscous Burgers rheology and ignores along-strike variations associated with changes in the age and hence thermal state of the incoming plate. We also assume the viscosity values of the mantle wedge to be lower than those of the oceanic mantle by an order of magnitude to account for the presence of H_2O and melts (Wang et al., 2012). Our mantle-wedge steady-state (Maxwell) viscosity is lower than that inferred by Lorenzo-Martín et al. (2006) mainly because of the presence of a subducting slab in our model. The material property values are shown in Fig. 1b. The stagnant and cold part of the mantle wedge recognized in thermal and seismic studies (Wada and Wang, 2009; Abers et al., 2017) is represented by an elastic wedge corner (the "cold nose" in Fig. 1b). The model accommodates actual fault and slab geometry and long-wavelength surface topography and approximately includes the effect of gravity using a prestress advection approach (Peltier, 1974).

3.2. A model of enhanced locking

The rapidity and the spatial scale of the observed GNSS velocity change outlined in section 2 point to an increase in the locking of the megathrust, but the inferred degree of such an increase depends on the rate of crustal deformation prior to the increase. Models for the prior deformation rate are not very well constrained by the available sparse data, but they should fit the first few years of the east–west component of the observed COYQ time series (Fig. 3a). We consider two options. First, in this section, we describe modelling of the prior crustal deformation rate using a postseismic deformation model based on the coseismic slip distribution of Ho et al. (2019). Second, in the next section, we describe modelling based on the slip distribution of Moreno et al. (2009) but also introduce a hypothetical slow slip event in order to match the prior rate of COYQ.

The great 1960 earthquake caused extensive crustal deformation and generated a large tsunami. Previous models of its coseismic slip distribution were based mainly on data reported by Plafker and Savage (1970) including field measurements of coastal uplift and subsidence and limited geodetic measurements (triangulation and levelling) before and after the earthquake. These models typically feature much less coseismic slip in the southern half of the rupture zone than in the northern half and very little slip near the trench (e.g., Moreno et al., 2009). Recently, Ho et al. (2019) incorporated numerous tsunami records in a new study of the 1960 earthquake slip and greatly improved offshore resolution. They reported that the northern and southern halves of the rupture zone underwent roughly the same amount of slip and that much slip occurred near the trench. We construct a postseismic deformation model that invokes the coseismic slip distribution of Ho et al. (2019) but is otherwise the same as the model of Sun et al. (2018). Fig. 6 shows postseismic deformation at COYQ predicted by this model, and Fig. 7a shows its predicted regional deformation pattern, both in comparison to observations. We es-

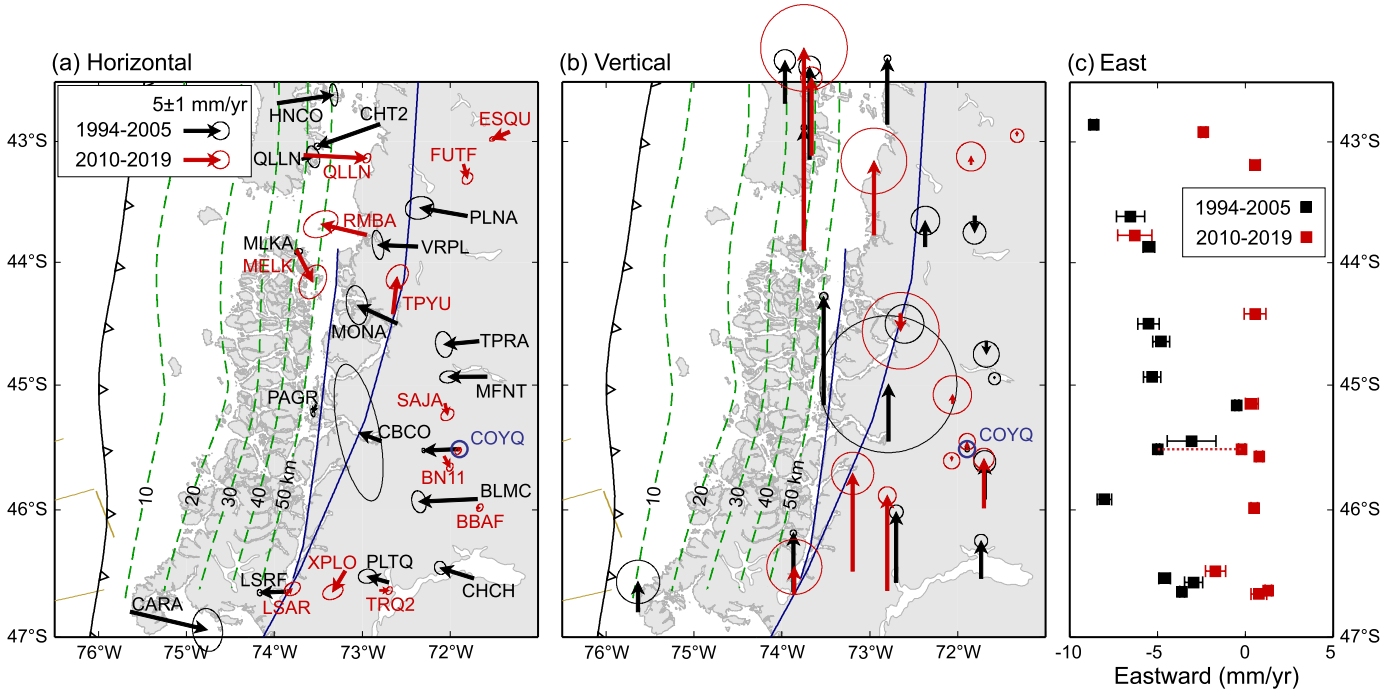

Fig. 5. Regional change in GNSS velocity in the early 21st century. Error ellipse or bar represents 3 standard deviations. (a) New horizontal velocities (red) based on continuous GNSS data during 2010–2019 (Table B2) in comparison with the earlier velocities reported by Wang et al. (2007) based on 1994–2005 campaign data. At COYQ (blue circle), the earlier velocity was based on data until 2006, and the new velocity is based on data since 2013 after correction for the 2016 earthquake (Figs. 3 and 6). As in Fig. 2a, sites west of LOFZ (blue lines) have been corrected for strike-parallel sliver motion. (b) The vertical component. Same scale as in (a), with the error bar represented by a circle. (c) East component of the velocities as a function of latitude. The old and new COYQ values are connected with a red dotted line. For clarity, the plot only shows sites east of the 50 km depth contour of the plate interface.

chew a serious effort to fit GNSS site velocities near the southern boundary of the study area, where a slab window is well developed in association with the Chile ridge subduction (Russo et al., 2010a; 2010b) (Fig. 7). Seismic velocities at asthenospheric depths in the slab window are ∼ 3% slower than expected, even relative to seismic velocity models that include a slow asthenosphere, indicating a warmer geotherm and lower viscosity. This lower viscosity associated with the slab window is most likely responsible for the observed high trenchward velocities of the southernmost GNSS sites. This effect cannot be addressed by our postseismic deformation model which for simplicity ignores along-strike viscosity variations, but it will be an important subject for future research.

The simplest way to introduce enhanced interplate locking is to assume that the locked zone of the megathrust became wider in the downdip direction during our observation period (Fig. 7b). We assume that the degree of locking began to increase linearly with time in the first few years of the century (Fig. 6) and reached a peak value > 50 mm/yr in seven years in the southern portion of the study region (Fig. 7b). The enhanced locking (Fig. 7b) can explain the regional increase in eastward velocity (Figs. 5c). The incremental uplift predicted by this model (Fig. 7b) is also consistent with the observed change (Fig. 5b, the difference between the grey and red arrows). We do not attempt to fit the new velocity vectors shown in Fig. 5a or the velocity change shown in Fig. 5c site by site for the following reasons: (1) The distributions of GNSS stations that recorded the 1994–2005 and 2010–2019 velocities are different. (2) Most of the site velocities were based on observations of rather short time span (Table B2), and therefore uncertainties are large. (3) The GNSS stations were operational at different times, and thus site velocities are derived from somewhat different time periods between 2010–2019.

The regional data shown in Fig. 5 illustrate the rapidity of the increase in eastward velocity but do not show when the increase began. The COYQ time series can provide information on the onset time of the enhanced locking, but the data suffers from uncertainties associated with the data gaps during 2005–2007. The offset correction added in 2007 (section 2.1) affects the estimated onset time of the enhanced locking. Our preferred model shown in Fig. 6a is based on adding an offset of 4 mm to the west (i.e., downward shift of the time series). In this model, the enhanced locking started in 2003. If the offset is zero or twice as large (Fig. 3a), the model onset time will be 2002 (Fig. 6b) or 2004 (Fig. 6c), respectively. Regardless of the uncertainties in the onset time, enhanced downdip locking can readily explain the rapid increase in eastward velocity both at COYQ (Fig. 6) and at the regional scale (Figs. 5c and 7b).

3.3. A model of slow slip followed by enhanced locking

Given uncertainties in the coseismic slip models based on data prior to modern space geodesy, we also consider the postseismic deformation model of Sun et al. (2018) assuming validity of the coseismic slip distribution of Moreno et al. (2009). In this model, the westward velocity in the first few years of the century is smaller than observed at COYQ (Fig. 8), but a higher velocity can be obtained by assuming that a slow slip event (SSE) occurred on the megathrust around the turn of the century. So-called long-term SSEs lasting several years downdip of locked seismogenic zones have been detected in the Nankai, Mexico, Hikurangi, and Alaska subduction zones (e.g., Obara, 2011; Kostoglodov et al., 2010; Wallace and Beavan, 2010; Li et al., 2016). Low-frequency seismic tremor is usually abundant downdip of, but not in synchronization with, the long-term SSEs (Gao and Wang, 2017). We thus produced a model that includes such a long-term SSE just north of the CTJ, referred to as "Sun et al. + SSE" in Fig. 8. The location of the assumed SSE slip patch is compatible with the tremor distribution during 2005–2007 determined by Ide (2012) using a method of envelope correlation (Fig. 9a). Tremor sources during 2004–2007 had

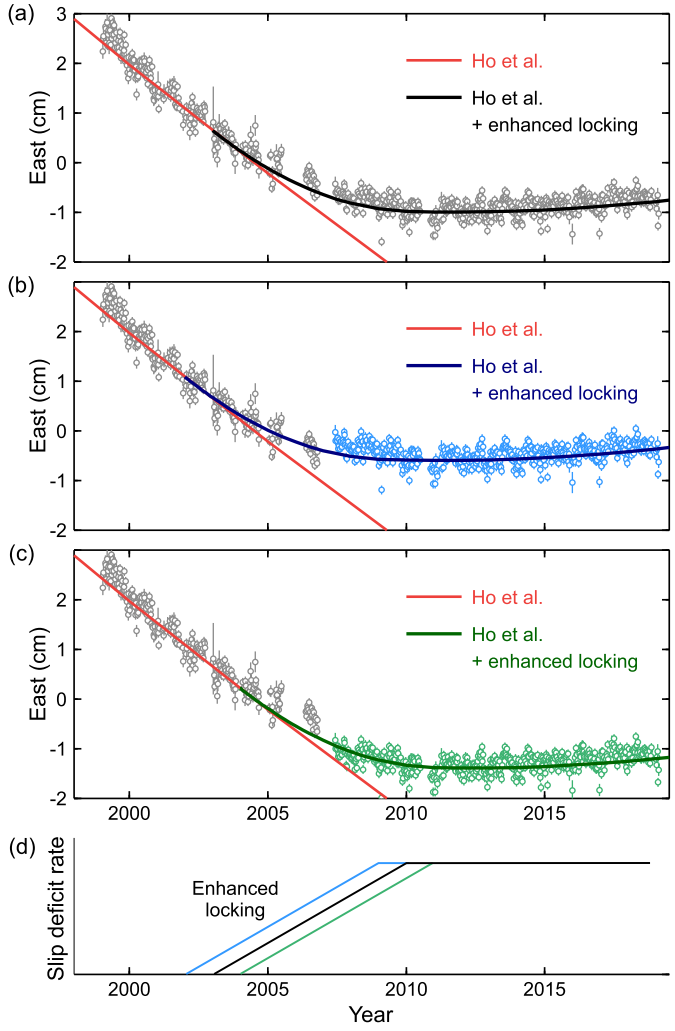

Fig. 6. Rapid decrease in west velocity with respect to SA (Fig. 4) at GNSS site COYQ in the early 21st century explained with a model of enhanced megathrust locking. The 3.85 mm offset caused by the 2016 earthquake visible in Fig. 3a has been removed. The model-predicted site motion prior to the onset of the enhanced locking is based on a postseismic deformation model using the coseismic slip distribution of Ho et al. (2019) (Fig. 7a). The distribution of enhanced locking is shown in Fig. 7b. (a) Preferred model in which a 2007 correction of −4 mm is made to the GNSS data. (b) No 2007 correction is made. (c) The 2007 correction is −8 mm. (d) Schematic illustration of the event history and how the inferred onset time of the enhanced locking is affected by the 2007 correction. Blue, black, and green are for corrections 0, −4, and −8 mm, respectively.

been determined by Gallego et al. (2013) using a source-scanning algorithm, although their location uncertainties are large (Fig. 9a). The assumed SSE can produce a westward site velocity at COYQ prior to 2005 as high as observed.

Our modelling shows that the termination of the SSE would not be sufficient to cause the observed regional increase in eastward site velocities shown in Fig. 5c. It suffices to use one example, with an offset of 4 mm in 2007 as in Fig. 6a, to illustrate this point. In this example, shown in Fig. 8 as "Sun et al. + SSE + enhanced locking", enhanced locking occurs after the SSE termination. Note that a fraction of the pre-2005 westward regional velocity is attributable to the SSE, and therefore the required increase in the degree of locking after SSE termination is less than that shown in the preferred model (Fig. 6a). The distribution of the locking increase is shown in Fig. 9b, together with resultant velocity increases in both the horizontal and vertical directions. Again, for reasons explained in section 3.2, we focus on the overall pattern of the velocity increase but do not attempt to fit the observed values site by site.

3.4. Discussion of enhanced locking

A number of trade-offs are apparent even in our highly simplified modelling of the southern 1960 earthquake rupture region. For example, the assumption of a narrower zone of enhanced locking in the downdip direction would necessarily entail a large increase in slip deficit rate, and vice versa. If we invoke along-strike variations in mantle viscosity in the postseismic deformation model of the 1960 earthquake, we can obtain different background locking patterns for the megathrust. These trade-offs in model parameters are indicative of the non-uniqueness of the modelling results. Nonetheless, the range of results stemming from reasonable values of model parameters cannot explain our observations unless we introduce a sudden downdip increase in megathrust locking, regardless of other model details.

An increase in megathrust locking during postseismic or interseismic deformation is not an entirely novel concept. In fact, all SSEs must terminate by an increase in fault locking. However, our modelling demonstrates that the termination of a presumed SSE is insufficient – by itself – to cause the observed regional GNSS velocity change (Fig. 8), and an additional increase in locking is required to match the observations (Fig. 9).

A sudden increase in landward GNSS velocities near a subduction zone has occasionally been reported elsewhere and interpreted to be caused by an increase in megathrust locking. The 2014 Mw 8.1 Iquique earthquake in northern Chile was reported to have increased GNSS velocities in an area south of the rupture (Hoffmann et al., 2018), although the velocity increase may alternatively be attributed to the diminishing viscoelastic postseismic deformation of the 2007 Mw 7.8 Tocopilla earthquake in the area. A small area in southernmost Cascadia was observed to accelerate after a nearby Mw 6.8 earthquake in the incoming oceanic plate (Materna et al., 2019). In both cases, the GNSS velocity change is limited in the forearc area, and the inferred locking increase is thought to be a response to a preceding large earthquake. In contrast, the GNSS velocity change reported in this paper extends far into the back arc, and there is no preceding large earthquake near the inferred zone of locking increase.

Enhanced downdip locking in our preferred model (Figs. 6 and 7) can be viewed as a substantial deceleration of very long-lasting, slow, and deep afterslip following the 1960 earthquake. This is in contrast with a phenomenon recently observed at the Japan Trench subduction zone, where a large patch of the Pacific–Japan megathrust downdip of the then-future 2011 Mw 9 Tohoku-oki earthquake rupture exhibited accelerated slip for about a decade leading up to the 2011 earthquake (Mavrommatis et al., 2014; Yokota and Koketsu, 2015; Wang et al., 2018). The temporal changes in the megathrust locking state downdip of the main seismogenic zone without an apparent triggering mechanism seen in the Chile and Japan Trench subduction zones, either before or after a giant earthquake, presents new challenges to the understanding of fault mechanics and subduction zone dynamics. The spatial relationship between increased locking and tremor distribution (Fig. 9) also deserves investigation.

Based on geological and geodetic observations around latitude 43.5°S, within the northern part of our study area, Melnick et al. (2018) proposed that the rupture zone of the 1960 earthquake in that area became increasingly locked from the time of the earthquake to 2005. If true, it can be regarded a slow healing process of the megathrust seismogenic zone. Our observation further south in the 1960 rupture region is an increase in megathrust locking that occurred further downdip and much later. Whether there is any tectonic link between the processes proposed in these two studies is a matter of conjecture.

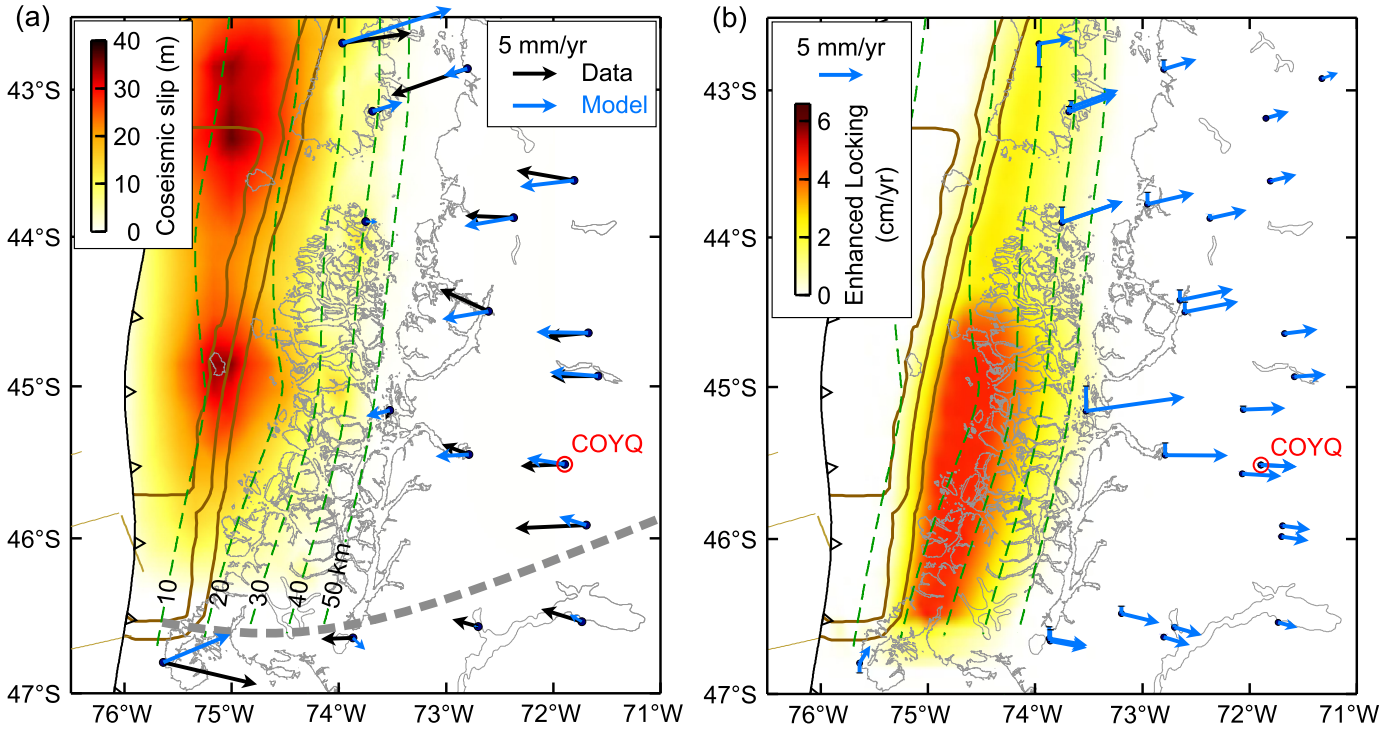

Fig. 7. Regional map view of the enhanced locking model and site velocities prior to the locking increase. (a) Prior site velocities predicted by a viscoelastic postseismic deformation model that invokes the shown Ho et al. (2019) coseismic slip distribution but otherwise is the same as the model of Sun et al. (2018), in comparison with the 1994–2005 data. Large misfit at the southernmost sites is due to the use of a simplified model of along-strike uniform viscosity that ignores the presence of a slab window, of which the northern boundary is approximately delineated by the thick dashed line (Russo et al., 2010b). (b) Predicted velocity change, shown at all the GNSS sites, due to the assumed enhanced locking as seen in 2015 to explain the regional increase in eastward velocity shown in Fig. 5c. The vertical component (bar at each site) is for visual comparison with the difference between the old and new values shown Fig. 5b. See Fig. 6 for possible onset times of the locking increase.

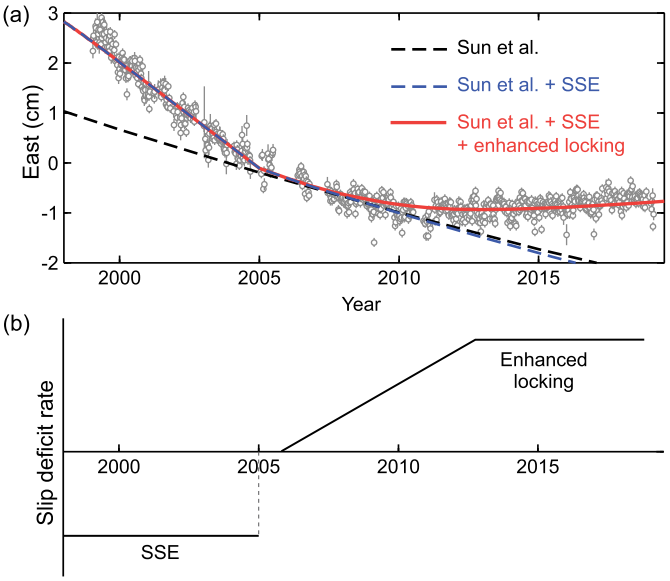

Fig. 8. An alternative to the model of Figs. 6 and 7 seen at COYQ: An SSE followed by enhanced locking. (a) Model predictions at COYQ in comparison with the time series shown in Fig. 6a. The 1960 postseismic deformation model is that of Sun et al. (2018), but the faster motion before ~ 2005 is caused by an assumed slow slip event on the megathrust (Fig. 9a). The distribution of locking increase is shown in Fig. 9b. (b) Schematic illustration of the event history.

4. Conclusions

Viscoelastic relaxation of the stresses induced by the Mw 9.5 1960 Chile earthquake causes geodetically observable deformation that may last a century. However, by analysing GNSS observations made 4 to 6 decades after the earthquake, we found a remarkable rapid change in site velocities in the early 21st century that cannot be explained by the viscoelastic postseismic deformation alone. We have thus proposed a conceptual model of enhanced megathrust locking and demonstrated the feasibility of the concept using simple numerical models. The main conclusions of the work are as follows.

(1) A comparison of continuous GNSS data of 2010–2019 with campaign data of 1994–2005 reveals an unexpected systematic increase in landward (east) motion velocity over a large region covering the latitudinal range of the southern half of the great 1960 Chile earthquake rupture (Fig. 5c). The only long-lived continuous GNSS site (COYQ), situated over 200 km from the 1960 rupture zone, indicates that this change rapidly occurred within a few years before 2010 (Fig. 3a).

(2) The best, and likely the only, explanation for the rapid regional increase in the landward velocity is a widening of the megathrust locked zone in the downdip direction beginning around 2003 (Figs. 6 and 7). The rapidity of the GNSS velocity change cannot be explained without invoking this increased locking, although details of the increase such as the width, magnitude, and along-strike distribution are affected by uncertainties in the 1960 earthquake coseismic slip model, mantle rheology, and the possible occurrence of SSEs. This temporal change in the megathrust locking state presents new challenges to the understanding of fault mechanics and subduction zone dynamics.

(3) The seaward (west) motion of COYQ, and to some degree of some other sites, prior to the enhanced locking is faster than predicted by previously published viscoelastic postseismic deformation models for the 1960 earthquake. The faster motion can be explained either by invoking greater coseismic slip in

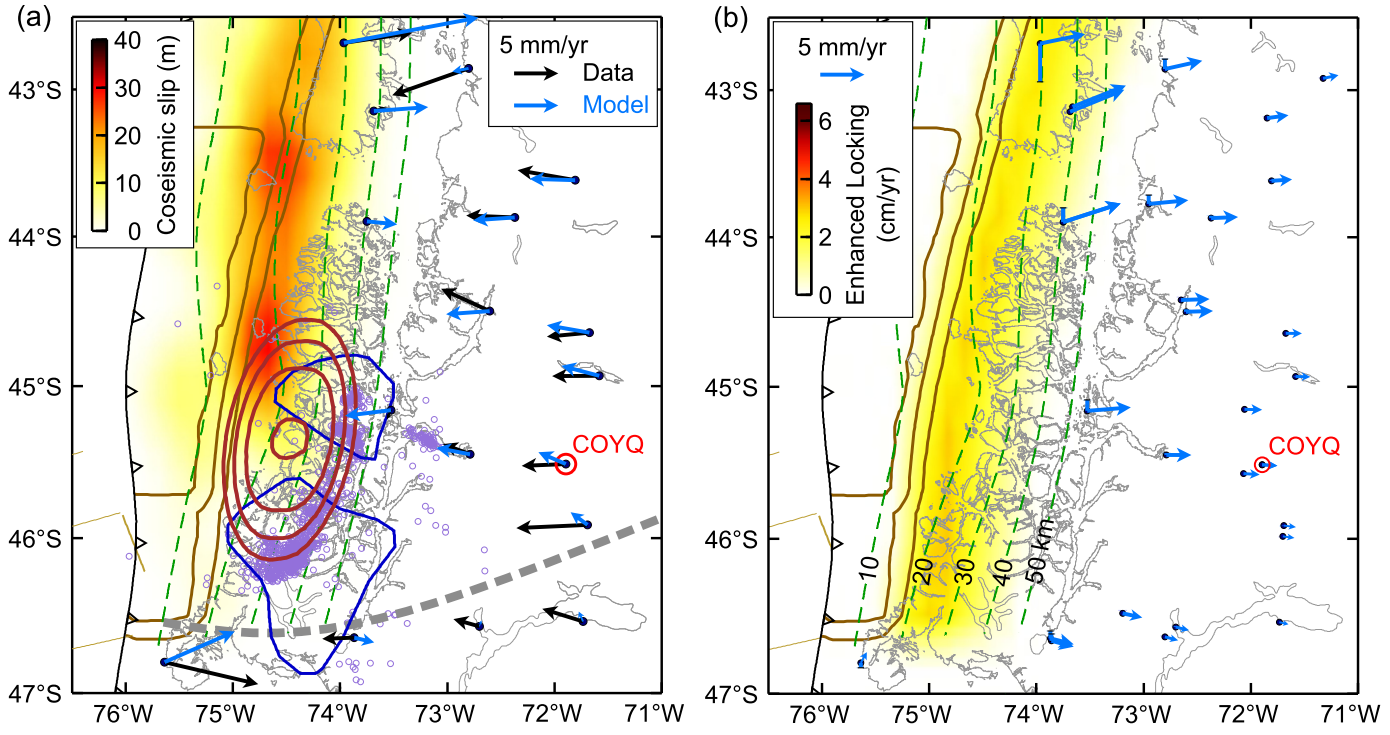

Fig. 9. Regional map view of the model shown in Fig. 8. (a) Velocities as seen in 2005 predicted with the Sun et al. model plus an elliptical SSE during 1998–2005, in comparison with the 1994–2005 data. Thick dashed line approximately delineates the northern boundary of a slab window (Russo et al., 2010b). Neglect of the slab window may explain the large misfit at the southernmost sites. The shown 1960 coseismic slip distribution is from Moreno et al. (2009) and was used in the Sun et al. (2018) model. The SSE (pure thrust) is contoured in red at 1 cm. Tectonic tremor sources during 2005–2007 reported by Ide (2012) are shown as purple circles, and the tremor areas for 2004–2007 reported by Gallego et al. (2013) are outlined using blue lines. (b) Similar to Fig. 7b, but the enhanced locking is over a narrower depth range and assumed to have occurred after the SSE (Fig. 8).

the southern part of the 1960 earthquake rupture area as recently reported by Ho et al. (2019) (Fig. 6) or by assuming the occurrence of a long-term SSE (Fig. 8). The latter is an arbitrary assumption but is compatible with observed distribution of tectonic tremor in this area (Gallego et al., 2013; Ide, 2012; Sáez et al., 2019).

Declaration of competing interest

The authors declare that they have no known competing financial interests or personal relationships that could have appeared to influence the work reported in this paper.

Acknowledgements

We thank Sergio Barrientos and Juan Carlos Baez of Universidad de Chile, for discussions and in-country support during fieldwork. Gonzalo Hermosilla of SERNAGEOMIN, Coyhaique, helped with field logistics. Sr. Pablo Keupuchur, Ian Farmer, Don Gustavo, Senora Cristina López Quintana, and Sr. Raul Tarnovschi provided field support. Sra. Andreea Bahamonde Valenzuela, Sr. Adrián Escobar, and Sra. Gabriela Gomez, and the National Park Guards at Laguna San Rafael, all of the Chilean Corporación Nacional Forestal (CONAF), aided with permitting and logistics. Don Cirilo, Sr. Oscar Molinos, Sr. Artemio Perez, and Sr. Isidro Bastide Rivas gave permission to install and maintain GNSS stations on their properties. Hans van der Marel of TU Delft and George Slad, Greg Chavez, and Noel Barstow of IRIS PASSCAL helped design and operate station power setup. TU Delft provided equipment and most of the funding for the fieldwork. Author contributions: Russo led the collaboration. Bevis initiated an early phase of the collaboration and independently processed the COYQ data for calibration. Ambrosius processed all the GNSS data. Mocanu, Russo, Fernandes, and Ambrosius carried out field work. Luo did the modelling. Luo and Ambrosius drafted the figures. Wang led the scientific interpretation and drafted most of the text. All the authors contributed to the writing of the paper. Reviewers Roland Bürgmann and Takeshi Sagiya provided valuable comments and suggestions.

Appendix A. Decomposition of signals in COYQ time series

The COYQ time series displayed in Fig. 3 include such signals as annual seasonal variations and earthquake perturbations that are largely extraneous to our results and do not affect our analysis. Nonetheless, for completeness, it is useful to quantify these signals. We use the following function to fit the COYQ position data to parameterize the various signals:

$$f(t) = C\sin(\theta) + D\cos(\theta) + \sum_{n=0}^{N} A_n + B_n(t - T_n) + E_n\left[1 - \exp\left(-\frac{t - T_n}{\tau_n}\right)\right] \quad (A.1)$$

where N is the total number of earthquakes considered ($= 3$ in this work), C, D, are amplitudes of the annual variations, and θ includes time and the one-year period. T_n and A_n ($n = 0, \ldots N$) are the time and value, respectively, of position reference or earthquake-induced offset, and E_n, τ_n, are coefficients for the exponential term. The beginning phase of the time series is $n = 0$; for example, T_0 is the date of our first data point in 1999, and A_0 is its reference position. $n = 1$, 2, and 3 denote the 2010 Maule, 2015 Illapel, and 2016 Quellón earthquakes, respectively. The signals most relevant to our purpose are represented mostly, but not fully, by the linear and exponential terms for $n = 0$. Obviously, the geodynamic discussion in this paper is adequately based on the

"raw" time series in Fig. 3 and does not reply on any of the terms in the above function. A possible offset related to station repair in 2007 is not included in this function.

When fitting this function to the COYQ time series, we searched for the optimal values of τ_n using an iterative scheme that minimizes the root-mean-square (RMS) misfit. We obtained the other parameters using a simpler least-squares fitting approach. The parameters thus determined are listed in Table B1. The only visually recognizable coseismic offset in Fig. 3a is the westward jump $A_3 = 3.85$ mm caused by the 2016 Quellón earthquake. It has been removed from the time series shown in Figs. 6 and 8.

Appendix B. Supplementary material

Supplementary material related to this article can be found online at https://doi.org/10.1016/j.epsl.2020.116200.

References

Abers, G.A., van Keken, P.E., Hacker, B.R., 2017. The cold and relatively dry nature of mantle forearcs in subduction zones. Nat. Geosci. 10, 333–337. https://doi.org/10.1038/NGEO2922.

Amos, C.B., Audet, P., Hammond, W.C., Burgmann, R., Johanson, I.A., Blewitt, G., 2014. Uplift and seismicity driven by groundwater depletion in central California. Nature 509, 483–486.

Argus, D.F., Gordon, R.G., Heflin, M.B., Ma, C., Eanes, R.J., Willis, P., Peltier, W.R., Owen, S.E., 2010. The angular velocities of the plates and the velocity of the Earth's center from space geodesy. Geophys. J. Int. 180, 913–960.

Bertiger, W., Desai, S.D., Haines, B., Harvey, N., Moore, A.W., Owen, S., Weiss, J.P., 2010. Single receiver phase ambiguity resolution with GPS data. J. Geod. 84, 327–337.

Blewitt, G., Hammond, W.C., Kreemer, C., 2018. Harnessing the GPS data explosion for interdisciplinary science. Eos Trans. AGU 99. https://doi.org/10.1029/2018EO104623.

Brooks, B.A., Bevis, M., Smalley Jr, R., Kendrick, E., Manceda, R., Lauría, E., Maturana, R., Araujo, M., 2003. Crustal motion in the Southern Andes (26°–36°S): Do the Andes behave like a microplate? Geochem. Geophys. Geosyst. 4 (10), 1085. https://doi.org/10.1029/2003GC000505.

Cembrano, J., Lavenu, A., Reynolds, A., Arancibia, G., Lopez, G., Sanhueza, A., 2002. Late Cenozoic transpressional ductile deformation north of the Nazca–South America–Antarctica triple junction. Tectonophysics 354, 289–314.

Cifuentes, I.L., 1989. The 1960 Chilean earthquakes. J. Geophys. Res. 94, 665–680.

Barrientos, S., Ward, S., 1990. The 1960 Chile earthquake: inversion for slip distribution from surface deformation. J. Geophys. Res. 103, 589–598.

Dietrich, R., Ivins, E.R., Casassa, G., Lange, H., Wendt, J., Fritsche, M., 2010. Rapid crustal uplift in Patagonia due to enhanced ice loss. Earth Planet. Sci. Lett. 289, 22–29.

Gallego, A., Russo, R.M., Comte, D., Mocanu, V., Murdie, R.E., VanDecar, J.C., 2013. Tidal modulation of continuous nonvolcanic seismic tremor in the Chile triple junction region. Geochem. Geophys. Geosyst. 14, 851–863. https://doi.org/10.1002/ggge.20091.

Gao, X., Wang, K., 2017. Rheological separation of the megathrust seismogenic zone and Episodic Tremor and Slip. Nature 543, 416–419. https://doi.org/10.1038/nature21389.

Hayes, G.P., Wald, D.J., Johnson, R.L., 2012. Slab1.0: a three-dimensional model of global subduction zone geometries. J. Geophys. Res., Solid Earth 117 (B1).

Hoffmann, F., Metzger, S., Moreno, M., Deng, Z., Sippl, C., Ortega-Culaciati, F., Oncken, O., 2018. Characterizing afterslip and ground displacement rate increase following the 2014 Iquique–Pisagua Mw 8.1 earthquake, Northern Chile. J. Geophys. Res., Solid Earth 123, 4171–4192. https://doi.org/10.1002/2017JB014970.

Kendrick, E., Bevis, M., Smalley Jr., R., Brooks, B., 2001. An integrated crustal velocity field for the central Andes. Geochem. Geophys. Geosyst. 2 (11). https://doi.org/10.1029/2001GC000191.

Khazaradze, G., Wang, K., Klotz, J., Hu, Y., He, J., 2002. Prolonged post-seismic deformation of the 1960 great Chile earthquake and implications for mantle rheology. Geophys. Res. Lett. 29, 71–74.

Klotz, J., Khazaradze, G., Angermann, D., Reigber, C., Perdomo, R., Cifuentes, O., 2001. Earthquake cycle dominates contemporary crustal deformation in Central and Southern Andes. Earth Planet. Sci. Lett. 193, 437–446.

Kostoglodov, V., Husker, A., Shapiro, N.M., Payero, J.S., Campillo, M., Cotte, N., Clayton, R., 2010. The 2006 slow slip event and nonvolcanic tremor in the Mexican subduction zone. Geophys. Res. Lett. 37, L24301.

Kreemer, C., Zaliapin, I., 2018. Spatiotemporal correlation between seasonal variations in seismicity and horizontal dilatational strain in California. Geophys. Res. Lett. 45, 9559–9568. https://doi.org/10.1029/2018GL079536.

Ho, T.C., Satake, K., Watada, S., Fujii, Y., 2019. Source estimate for the 1960 Chile earthquake from joint inversion of geodetic and transoceanic tsunami data. J. Geophys. Res., Solid Earth 124, 2812–2828. https://doi.org/10.1029/2018JB016996.

Hu, Y., Wang, K., He, J., Klotz, J., Khazaradze, G., 2004. Three-dimensional viscoelastic finite element model for postseismic deformation of the great 1960 Chile earthquake. J. Geophys. Res. 109. https://doi.org/10.1029/2004JB003163.

Ide, S., 2012. Variety and spatial heterogeneity of tectonic tremor worldwide. J. Geophys. Res. 117, B03302. https://doi.org/10.1029/2011JB008840.

Li, S., Freymueller, J., McCaffrey, R., 2016. Slow slip events and time-dependent variations in locking beneath Lower Cook Inlet of the Alaska–Aleutian subduction zone. J. Geophys. Res. 121. https://doi.org/10.1002/2015JB012491.

Lorenzo-Martín, F., Roth, F., Wang, R., 2006. Inversion for rheological parameters from post-seismic surface deformation associated with the 1960 Valdivia earthquake, Chile. Geophys. J. Int. 164, 75–87.

Materna, K., Bartlow, N., Wech, A., Williams, C., Bürgmann, R., 2019. Dynamically triggered changes of plate interface coupling in Southern Cascadia. Geophys. Res. Lett. 46, 12,890–12,899. https://doi.org/10.1029/2019GL084395.

Mavrommatis, A.P., Segall, P., Johnson, K.M., 2014. A decadal-scale deformation transient prior to the 2011 Mw 9.0 Tohoku-oki earthquake. Geophys. Res. Lett. 41, 4486–4494. https://doi.org/10.1002/2014GL060139.

Melnick, D., Li, S., Moreno, M., Cisternas, M., Jara-Muñoz, J., Wesson, R., Nelson, A., Báez, J.C., Deng, Z., 2018. Back to full interseismic plate locking decades after the giant 1960 Chile earthquake. Nat. Commun. 9, 3527. https://doi.org/10.1038/s41467-018-05989-6.

Moreno, M.S., Bolte, J., Klotz, J., Melnick, D., 2009. Impact of megathrust geometry on inversion of coseismic slip from geodetic data: application to the 1960 Chile earthquake. Geophys. Res. Lett. 36. https://doi.org/10.1029/2009GL039276.

Moreno, M., Melnick, D., Rosenau, M., Bolte, J., Klotz, J., Echtler, H., Baez, J., Bataille, K., Chen, J., Bevis, M., Hase, H., 2011. Heterogeneous plate locking in the South–Central Chile subduction zone: building up the next great earthquake. Earth Planet. Sci. Lett. 305, 413–424. https://doi.org/10.1016/j.epsl.2011.03.025.

Obara, K., 2011. Characteristics and interactions between non-volcanic tremor and related slow earthquakes in the Nankai subduction zone, southwest Japan. J. Geodyn. 52, 229–248.

Peltier, W.R., 1974. The impulse response of a Maxwell Earth. Rev. Geophys. Space Phys. 12, 649–668.

Plafker, G., Savage, J., 1970. Mechanism of the Chilean earthquakes of May 21 and 22, 1960. Geol. Soc. Am. Bull. 81, 1001–1030.

Pritchard, M.E., Simons, M., 2006. An aseismic slip pulse in northern Chile and along-strike variations in seismogenic behaviour. J. Geophys. Res. 111, B08405.

Richter, A., Ivins, E., Lange, H., Mendoza, L., Schröder, L., Hormaechea, J.L., Casassa, G., Marderwald, E., Fritsche, M., Perdomo, R., Horwath, M., 2016. Crustal deformation across the Southern Patagonia icefield observed by GNSS. Earth Planet. Sci. Lett. 452, 206–215. https://doi.org/10.1016/j.epsl2016.07.042.

Rodell, M., Famiglietti, J.S., Wiese, D.N., Reager, J.T., Beaudoing, H.K., Landerer, F.W., Lo, M.-H., 2018. Emerging trends in global freshwater availability. Nature 557, 651–659. https://doi.org/10.1038/s41586-018-0123-1.

Russo, R.M., VanDecar, J.C., Comte, D., Mocanu, V.I., Gallego, A., Murdie, R.E., 2010a. Subduction of the Chile Ridge: upper mantle structure and flow. GSA Today 20. https://doi.org/10.1130/GSATG61A.1.

Russo, R.M., Gallego, A., Comte, D., Mocanu, V.I., Murdie, R.E., VanDecar, J.C., 2010b. Source-side shear wave splitting and upper mantle flow in the Chile Ridge subduction region. Geology 38, 707–710.

Sáez, M., Ruiz, S., Ide, S., Sugioka, H., 2019. Shallow nonvolcanic tremor activity and potential repeating earthquakes in the Chile Triple Junction: seismic evidence of the subduction of the active Nazca–Antarctic spreading center. Seismol. Res. Lett. https://doi.org/10.1785/0220180394.

Sun, T., Wang, K., 2015. Viscoelastic relaxation following subduction earthquakes and its effects on afterslip determination. J. Geophys. Res. 120, 1329–1344. https://doi.org/10.1002/2014JB011707.

Sun, T., Wang, K., He, J., 2018. Crustal deformation following great subduction earthquakes controlled by earthquake size and mantle rheology. J. Geophys. Res. 123, 5323–5345. https://doi.org/10.1029/2017JB015242.

Sun, T., Wang, K., Iinuma, T., Hino, R., He, J., Fujimoto, H., Kido, M., Osada, Y., Miura, S., Ohta, Y., Hu, Y., 2014. Prevalence of viscoelastic relaxation after the 2011 Tohoku-oki earthquake. Nature 513, 84–87. https://doi.org/10.1038/nature13778.

Wada, I., Wang, K., 2009. Common depth of slab-mantle decoupling: reconciling diversity and uniformity of subduction zones. Geochem. Geophys. Geosyst. 10, Q10009.

Wallace, L.M., Beavan, J., 2010. Diverse slow slip behavior at the Hikurangi subduction margin, New Zealand. J. Geophys. Res. 115, B12402. https://doi.org/10.1029/2010JB007717.

Wang, K., Hu, Y., He, J., 2012. Deformation cycles of subduction earthquakes in a viscoelastic Earth. Nature 484, 327–332. https://doi.org/10.1038/nature11032.

Wang, K., Hu, Y., Bevis, M., Kendrick, E., Smalley Jr., R., Vargas, R.B., Lauría, E., 2007. Crustal motion in the zone of 1960 Chile earthquake: detangling earthquake-cycle deformation and forearc-sliver translation. Geochem. Geophys. Geosyst. 8, Q10010. https://doi.org/10.1029/2007GC001721.

Wang, K., Sun, T., Brown, L., Hino, R., Tomita, F., Kido, M., Iinuma, T., Kodaira, S., Fujiwara, T., 2018. Learning from crustal deformation associated with the M = 9

2011 Tohoku-oki earthquake. Geosphere 14, 552–571. https://doi.org/10.1130/GES01531.1.

Yokota, Y., Koketsu, K., 2015. A very long-term transient event preceding the 2011 Tohoku earthquake. Nat. Commun. 6, 5934. https://doi.org/10.1038/ncomms6934.

Zumberge, J.F., Heflin, M.B., Jefferson, D.C., Watkins, M.M., Webb, F.H., 1997. Precise point positioning for the efficient and robust analysis of GPS data from large networks. J. Geophys. Res. 102, 5005–5017.